Journal of Materials Chemistry C

RSC Publishing

PAPER

View Article Online
View Journal | View Issue

Cite this: J. Mater. Chem. C, 2013, 1, 5047

Regulation of luminescence band and exploration of antibacterial activity of a nanohybrid composed of fluorophore-phenothiazine nanoribbons dispersed with Ag nanoparticles†

Lin Kong,[a] Jia-xiang Yang,[a] Zhao-ming Xue,[a] Hong-ping Zhou,[a] Long-jiu Cheng,[a] Qiong Zhang,[a] Jie-ying Wu,[a] Bao-kang Jin,[a] Sheng-yi Zhang[a] and Yu-peng Tian*[ab]

Received 20th March 2013
Accepted 7th June 2013

DOI: 10.1039/c3tc30515e

www.rsc.org/MaterialsC

A D–π–A type phenothiazine derivative 4-((*E*)-2-(10-ethyl-10*H*-phenothiazin-3-yl)-vinyl)-benzaldehyde (abbreviated as **L**) was designed, synthesized and characterized by single crystal X-ray diffraction analysis. Dispersion-corrected theoretical calculation revealed that **L** molecules tend to grow along a 1-dimensional (1-D) orientation. Further, **L** was used to prepare nanohybrids consisting of silver nanoparticles (NPs) dispersed on **L** nanoribbons. **L** molecules coupled with Ag NPs through S atoms, which brought about a significant blue-shift of the fluorescence (FL) and an obvious increase of FL lifetime. Through fluorescence microscopy, the spectral change was used as a wavelength-based biodetection tool to study the possible mechanism for an enhanced inhibitory effect of **L**–Ag nanohybrids on both gram-negative bacterium *Escherichia coli* and gram-positive bacterium *Staphylococcus aureus* compared to either pure Ag NPs or pure **L**.

1 Introduction

Over the past few years, increasing attention has been devoted to understanding the interactions between organic and metallic components in organic–metal nanohybrids,[1] which can greatly improve the overall application performance of the nanohybrids, combine different properties into one material (such as electronic, magnetic, optical properties, and so on), and bring about new physical and/or biological properties.[2] Moreover, it has long been known that the structures at the organic–metal interface have some important influence on the properties of the nanohybrid. As a consequence, the molecular mechanisms in nanohybrids are important for understanding the functions of these materials and for the rational design of a functional nanohybrid. However, to the best of our knowledge, little research has been carried out about the factor in previous literature due to the lack of interface structure.

Silver NPs have been widely studied in a number of applications such as catalysis,[3] photocatalysis,[4] sensing,[5] surface enhanced Raman scattering (SERS)[6] and biomedical fields.[7] Silver in low concentration is nontoxic to human cells. Since ancient times, silver has been extensively employed to control spoilage and fight infections. In recent years, the antibacterial and antiviral actions of Ag NPs have been thoroughly investigated.[8] Moreover, the physical, chemical, and biological properties of Ag NPs can be designed and tuned by changing the size, shape and surface agents. Thiols, carboxylates, amides, imidazoles, indoles, hydroxyls and DNA oligonucleotides[9] are common organic compounds utilised to prepare Ag-based nanostructures, among which the interactions between Ag and S atoms are very strong, and as a consequence Ag/thiol nanostructures are widely investigated.[10]

Phenothiazine derivatives, which involve S atoms in the structure, bear a rigid conjugated plane and exhibit good hole and electron transporting properties. In many cases, phenothiazine groups can be employed as electron-donors, and can be used to prepare D–π–A type molecules (D = donor, A = acceptor) through linkage with an electron-acceptor group, which are regarded as ideal candidates for red emitting and nonlinear optical materials.[11] Furthermore, phenothiazine and its derivatives were traditionally used as antibacterial drugs and have a wide range of applications in the bacteriostatic field.[12] Recently, our group[13] has synthesized a number of phenothiazine

[a]Department of Chemistry, Key Laboratory of Functional Inorganic Materials of Anhui Province, Anhui University, Hefei 230039, P. R. China. E-mail: yptian@ahu.edu.cn; Tel: +86-551-63861279

[b]State Key Laboratory of Crystal Materials, Shandong University, Jinan 502100, P. R. China

† Electronic supplementary information (ESI) available: Preparation of intermediates **1** and **2**; XRD patterns of **L** single crystal; SEM images; the fragments selected for weak interactions; the UV-vis spectrum of phenothiazine; cyclic-voltammetric response of the phenothiazine fragment and $AgNO_3$; the comparison of the H NMR spectra of **L** and **L**–Ag nanohybrid; the Raman spectrum of the phenothiazine fragment; the effect of concentration of $AgNO_3$ on the formation of **L**–Ag nanohybrid; antibacterial effect (MIC). CCDC 930065. For ESI and crystallographic data in CIF or other electronic format see DOI: 10.1039/c3tc30515e

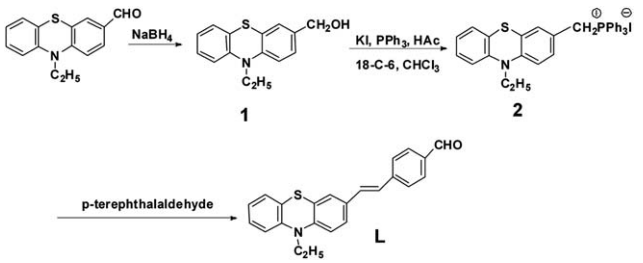

Scheme 1 Synthesis route of the target compound **L**.

derivatives with linear and nonlinear optical properties. In this study, we were interested in preparing nanohybrids from phenothiazine derivatives and silver NPs to achieve new optical and/or biological materials in which the two components could act synergistically[14] and adjust the properties.

Considering all the aspects above, a phenothiazine derivative, **L**, was designed and synthesized, in which the phenothiazine and benzene groups were employed as an electron-donor unit and the aldehyde group as an electron-acceptor unit. Therefore, phenothiazine, benzene groups and aldehyde units were linked by vinyl bonds to form a D–π–A type molecule (Scheme 1). Then, it was coupled with Ag NPs through a simple process at room temperature to get an **L**–Ag nanohybrid, which consisted of Ag NPs dispersed on the surface of **L** nanoribbons. The coupling effect between **L** and Ag components and the interface structure of the **L**–Ag nanohybrid were studied through NMR and Raman techniques. The energy transfer in the nanohybrid was studied from blue-shifted fluorescence and increased FL lifetime. The coupling effect between the two components also resulted in an obvious improvement of the antibacterial activity against both gram-negative bacterium *Escherichia coli* and gram-positive bacterium *Staphylococcus aureus*. The antibacterial activity of the **L**–Ag nanohybrid was superior to either pure **L** or pure Ag NPs. Through fluorescence microscopy, the blue-shifted fluorescence was used as a wavelength-based biodetection tool to study the possible mechanism for the enhanced inhibitory effect.

2 Experimental section

2.1 Preparation of L

The preparation of intermediates **1** and **2** is shown in the ESI.† After their preparation, terephthalaldehyde (0.08 g, 0.6 mmol) was dissolved in EtOH (20 mL) and added dropwise into intermediate **2** (0.32 g, 0.5 mmol)–EtOH (20 mL) solution. The above mixture was stirred overnight at room temperature and monitored by TLC to ensure complete reaction. Then, ethanol was evaporated, the residue was dissolved in 300 mL CH_2Cl_2 and washed three times with distilled water, and then dried over anhydrous magnesium sulfate overnight. The solvent was removed with a rotary evaporator. The residue was purified by column chromatography on silica gel with petroleum ether–ethyl acetate (50 : 1) as an eluent to get target compound **L** (0.14 g) in 80.4% yield. ^{1}H NMR (400 MHz, d_6-DMSO): δ (ppm) 9.97 (s, 1H); 7.89 (d, 2H, J = 8.0 Hz); 7.77 (d, 2H, J = 8.4 Hz); 7.47–7.45 (m, 2H); 7.38 (d, 1H, J = 16.4 Hz); 7.25 (d, 1H, J = 16.4 Hz); 7.21 (t, 1H, J = 8.0 Hz); 7.15 (d, 1H, J = 7.6 Hz); 7.03 (d, 2H, J = 8.0 Hz); 6.95 (t, 1H, J = 7.2 Hz); 3.94 (m, 2H (CH_2)); 1.31 (t, 3H (CH_3)). ^{13}C NMR (100 MHz): δ (ppm) 192.77, 144.19, 143.89, 135.22, 131.46, 131.23, 130.49, 128.21, 127.53, 127.38, 127.18, 125.99, 125.35, 122.67, 123.07, 123.57, 115.98, 41.72, 13.05. FT-IR (KBr cm^{-1}): 3054, 2925 (m), 1688 (m), 1593 (s), 1440 (s), 1188 (s), 714 (s).

Light yellow crystals of **L** suitable for X-ray diffraction were obtained by slow evaporation of **L**–DMF solution at room temperature for about 10 months.

2.2 Preparation of L–Ag nanohybrid

L–DMF solution (200 μL of 0.05 mol L^{-1}) was injected into 5 mL of high-purity water solution of $AgNO_3$ (1.70 mg, 0.01 mmol) under stirring. The mixture was stirred for 10 min and then left undisturbed for 12 h at room temperature for stabilization. During the process, the transparent solution gradually changes from light yellow to brown. The precipitate was centrifuged, washed with distilled water several times to remove excess inorganic salts and DMF, then dispersed into high-purity water, and the above solution was used for characterization and analysis.

Comparative experiments were also carried out. Pure Ag NPs were prepared according to the corresponding similar process in the absence of **L**. Pure **L** nanostructures were fabricated without inorganic salts. For preparing pure Ag NPs, $AgNO_3$ (1.70 mg, 0.01 mmol) was added to DMF–water (v_{DMF} : v_{water} = 200 μL : 5 mL) solvent mixture under stirring. For preparing pure **L** nanostructures, **L**–DMF solution (200 μL of 0.05 mol L^{-1}) was injected into 5 mL of high-purity water.

2.3 Bactericidal tests

To evaluate bactericidal activities of **L**–Ag nanohybrids, pure **L** nanostructures and pure Ag NPs, nutrient agar plates from a solution of agar were prepared. A 100 μL of bacterial suspension (*E. coli* and/or *S. aureus* with a concentration of 1.5 × 10^8 CFU mL^{-1}) was plated on a nutrient agar plate. Then, the disk containing **L**–Ag nanohybrids, **L** nanostructures or Ag NPs was gently placed on the center of the agar plates and incubated at 37 °C. After 24 h, bacterial colony growth was observed, and the zone of inhibition was measured to evaluate the antibacterial effect.

The minimum inhibitory concentration (MIC) was assessed using the standard dilution micromethod. The samples were diluted 2–1024 times with 100 μL of Mueller-Hinton broth inoculated with the tested bacteria (*E. coli* and/or *S. aureus*). The MIC was observed after 24 h of incubation at 37 °C. All of the bactericidal experiments were performed at room temperature and repeated three times; the measured data for each set of experiments were expressed with the average value.

2.4 Theoretical calculation

Molecular orbital calculations of time-dependent density functional theory (TD-DFT) at the B3LYP level basis set[15] were performed to study the electronic structures of **L**. Thermodynamic energy of weak interactions between adjacent molecules was also computationally calculated *via* M06/6-31+g(d,p) level basis set (Gaussian 09)[16] by varying the intermolecular position and

different packing models along *a*, *b* and *c* axes (Fig. S4†). The selected fragments were cut out directly from the CIF data. Single-point energy calculations were performed to obtain weak interaction energy between two relative fragments, which is defined as $E_{interaction} = E_{dimer} - 2E_{molecule\text{-}free}$. The data were corrected by basis set superposition error (BSSE).[17]

2.5 Characterization

The X-ray diffraction measurement of single crystal was performed on a Bruker SMART CCD area detector using graphite-monochromated Mo Ka radiation ($k = 0.71073$ Å) at 296(2) K. Intensity data were collected in the variable X-scan mode. The structures were solved by direct methods and difference Fourier syntheses. All non-hydrogen atoms were refined anisotropically and hydrogen atoms were introduced geometrically. Calculations were performed using the SHELXTL-97 program package.[18] The X-ray diffraction (XRD) patterns for nanomaterials were recorded on a MXP18AHF diffractometer using Cu Ka radiation ($\lambda = 1.54056$ Å) in the 2θ range from 10° to 70°. The morphologies were obtained on a field-emission scanning electron microscope (FESEM, Hitachi S-4800) and a transmission electron microscope (TEM, JEM-2100). The Raman spectra were recorded with a Labram-HR spectrometer using the 325 nm line of the Ar ion for excitation. UV-vis absorption spectra were obtained on a UV-3100 spectrophotometer in the wavelength range 300–600 nm. Fluorescence spectra were recorded at room temperature using a Hitachi F-7000 spectrophotometer. Fluorescence lifetime measurements were carried out using an HORIBA FluoroMax-4P fluorescence spectrometer equipped with a time-correlated single-photon counting (TCSPC) card. Fluorescence microscopy images were obtained from an Olympus IX-70 fluorescence microscope.

3 Results and discussion

3.1 Crystal structure of L

L crystallized in an orthorhombic form with space group *Pbca* as shown in Fig. 1. The crystallography data are summarized in Table 1. Selected bond lengths and bond angles are listed in the ESI Table S1.† In the molecule, the bond lengths of the benzene and phenothiazine ring were all of aromatic character. The linkage bond length between the benzene ring and the phenothiazine unit was quite conjugated with C15–C16 being 1.295(4) Å. The C15–C16 bond was nearly coplanar to the adjacent benzene and phenothiazine ring with the torsion angle of C9–C10–C15–C16 being −1.8(5)° and C16–C17–C18–C19 being ¬178.6(3)°. The structural features suggested that all nonhydrogen atoms were highly conjugated and nearly coplanar, which would favour the electronic delocalization in the whole molecule.

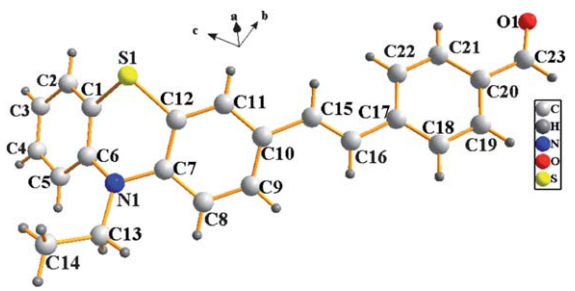

Fig. 1 Crystal structure of **L** with the atom numbering scheme.

3.2 Morphology of L nanostructure

L nanostructures were simply prepared from tetrahydrofuran (THF), ethanol (EtOH) and/or *N*,*N*-dimethylformamide (DMF) solution without addition of any template, catalyst and/or surfactant. SEM images of **L** self-assembly aggregates from DMF solution are shown in Fig. 2b. Nanoribbons were observed with lengths and diameters of micrometres and hundreds of nanometres, respectively. The morphologies of **L** prepared from the other two solvents also showed a one-dimensional structure (the images are shown in the ESI Fig. S2 and S3†).

3.3 Theoretical calculation

In order to explain the orientation growth of **L** molecules in micro size, thermodynamic principles were used through computational calculation of weak intermolecular interactions between adjacent molecules along *a*, *b* and *c* axes by varying the intermolecular position and different packing models. The selected fragments were cut out directly from the CIF data which are listed in the ESI Fig. S4.† The total energy and molecule–molecule assembling energy are listed in Table 2. The results showed that the dimer was two times lower in energy than the free molecule. The calculated assembling energy along the *a* axis was −52.44 kJ mol^{-1}, which was −14.56 kJ mol^{-1} along the *b* axis and −3.80 kJ mol^{-1} along the *c* axis, respectively. The result indicated that the interactions along the *a* axis were stronger than that along the other two, and the interactions along *a* and *b* directions were much stronger than that along the *c* axis. The result revealed that the interactions might lead to 1-D and/or semi 2-D orientation growth in nature (both in micro and macro size). The calculation results fitted well with the experimental data.

In order to verify the credibility of the above calculation, molecular orbital calculations of TD-DFT at the B3LYP level basis set were also performed to study the electronic structures of **L**, which are listed in the Section 3.5.1.

3.4 Formation of L–Ag nanohybrid

After detailed investigation on free **L** aggregation, the hybridization of **L** and Ag was further studied as follows. DMF was chosen as the solvent in the preparation because it is a strong reducing agent for silver ions. The **L**–Ag nanohybrid was prepared from DMF–H_2O solution containing **L** and $AgNO_3$, with no addition of any other materials. During the process, the assembly of **L** and the formation of Ag NPs occurred simultaneously. The XRD pattern (Fig. 2f) confirmed the existence of both the two components in the nanohybrid. The structure of Ag NPs was further determined from the high resolution transmission electron microscopy (HRTEM) images as shown in

Table 1 Crystal data and structure refinement for **L**[a]

Formula	C23H19NOS	Crystal system	Orthorhombic
Formula weight	357.45	Space group	*Pbca*
T (k)	296(2)	α/deg	90.00
a/Å	15.196(8)	b/Å	7.934(4)
c/Å	29.846(16)	Z	8
V/Å^3	3598(3)	Crystal size/mm	0.25 × 0.23 × 0.22
Calculated density (mg m^{-3})	1.320	F (000)	1504
Reflection collected	3351	Goodness of fit on F^2	1.031
R indices (all data)	$R_1 = 0.1129$	Final R indices [$I > 2\sigma(I)$]	$R_1 = 0.0515$
	w$R_2 = 0.1588$		w$R_2 = 0.1277$

[a] $R_1 = \Sigma||F_o| - |F_c||/\Sigma|F_o|$, w$R = [\Sigma w(F_o^2 - F_c^2)^2/\Sigma w(F_o^2)^2]^{1/2}$.

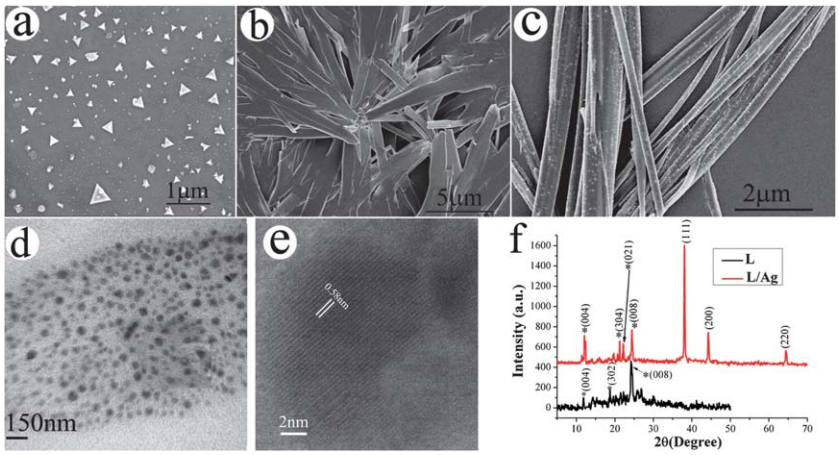

Fig. 2 Micrographs of (a) pure Ag NPs, (b) SEM of **L** nanoribbons obtained from DMF–H_2O solution, (c) SEM of the **L**–Ag nanohybrid, (d) TEM of Ag NPs in the **L**–Ag nanohybrid, (e) HRTEM of (d), and (f) XRD patterns of the as-prepared **L** nanoribbons and **L**–Ag nanohybrid.

Table 2 Total, assembling energies of **L** molecules along different directions at the M06/6-31+g(d,p) level

	Energy (Hartree)		Binding energy ΔE (kJ mol^{-1})
Axis	(Dimer)	(Molecule-free)	ΔE^a
a	−2829.873067196999	−1414.92654803	−52.44209491
b	−2829.858642247465		−14.5637021
c	−2829.854543502799		−3.800831786

[a] $\Delta E = E_{interaction} = E_{dimer} - 2E_{molecule\text{-}free}$.

Fig. 2e, which exhibited a single crystalline structure with a distinct lattice spacing of *ca.* 0.23 nm, corresponding well to the (111) plane of FCC Ag NPs.[19]

Compared with pure **L** nanoribbons, the length of **L** for the hybrid extended to tens of micrometres, indicating that **L** was affected during this process. On the other hand, Ag NPs were found to deposit in a near monodisperse manner on the surface of **L** nanoribbons with an average diameter of about 70 ± 12 nm (Fig. 2c), the morphology and size of which changed significantly from pure Ag NPs formed without **L** (Fig. 2a). For pure Ag NPs, there were irregular morphologies and particle sizes. Some of the Ag NPs had a triangular shape with an average size of ~200 nm. There were still a lot of small particles with uneven size. No usage of the surface active agent might be responsible for the phenomenon.

Furthermore, the XRD patterns of **L** and **L**–Ag nanohybrid (Fig. 2f) exhibited several peaks at the diffraction angles (10–20 degree), which gave evidence that the arrangement of **L** molecules was ordered in both **L** nanoribbons and the nanohybrid. In detail, for **L** nanoribbons, the main diffraction peaks located at 11.8° and 24.1°, corresponding to (004) and (008) planes, respectively (ESI Fig. S1†), which fitted well with the 1-D structure of pure **L**. Sharpness and strong intensity of the diffraction peaks reflected for (004) and (008) planes were also indicative of high crystallinity of **L** in the nanohybrid.

During the hybrid process, when **L**–DMF solution was injected into $AgNO_3$–water solution, Ag^+ might interact with **L** when they are mixed at the very beginning. Then, Ag^+ was reduced to Ag^0 by DMF. At the same time, **L** molecules precipitated. During this process, **L** served as a shape directing agent to guide the subsequent growth of Ag NPs, which drove Ag NPs to precipitate along with **L**. As a result, Ag NPs eventually dispersed on the surface of **L** nanoribbons. The morphology and size of Ag NPs for the nanohybrid were more regular than that of Ag NPs prepared without **L**, which revealed that **L**

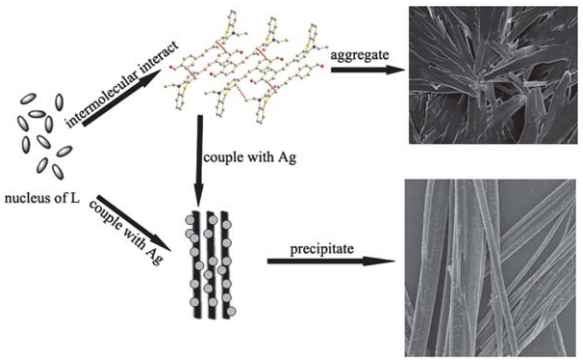

Fig. 3 A schematic representation of the formation of an **L**–Ag nanohybrid.

molecules played an important role in the formation of Ag NPs. Based on the results mentioned above, the formation process of the hybrid is presented in Fig. 3. **L** clusters self-assembled into a 1-D structure due to weak interactions between neighboring molecules. When $AgNO_3$ was introduced during the aggregation process, the assembly of **L** and the formation of Ag NPs occurred simultaneously and affected each other. Lastly, nanohybrids consisting of Ag NPs uniformly dispersed on **L** nanoribbons appeared.

3.5 Optical properties

From the results and discussion mentioned above, the interactions between the two components of the nanohybrid were somewhat strong and could bring about significant changes in morphology and/or size. Besides the morphology/size research, a more important goal in this work was to investigate the effect of the interactions on the optical properties. Indeed, when the nanohybrid formed, a blue-shift of absorption, a decrease of emission of **L** and the appearance of a new emission band were observed.

3.5.1 Absorption spectra. The UV-vis absorption spectrum of pure **L** nanoribbons exhibited two major absorption peaks at 320 nm and 404 nm (Fig. 4a), respectively. The latter corresponded to the HOMO–LUMO transition of **L** molecules, while the former resulted from the phenothiazine fragment as shown in Fig. S6.†[20]

The orbital features of **L** calculated using the TD-DFT method are presented in Fig. 6b, which might provide clues to understand the corresponding electronic structure of the excited-state and the energy matching status with Ag NPs. In the HOMO, the electrons were mainly concentrated on the electron-donor unit, while in the LUMO, the electrons were mainly concentrated on the electron-acceptor unit. Obviously, the electron transition from the HOMO to the LUMO was accompanied by charge transfer from the electron-donor unit to the electron-acceptor unit. The theoretical spectral characteristics showed two transitions (see ESI Table S2†). One was from the HOMO orbital to the LUMO (oscillator strength $f_{\mathrm{HOMO\text{–}LUMO}}$ being 0.3491) with λ_{abs} = 402 nm. The other was from the HOMO−1 orbital to the LUMO (oscillator strength $f_{(\mathrm{HOMO-1})\text{-}\mathrm{LUMO}}$ being 0.5140) with λ_{abs} = 317 nm. The results of theoretical calculation fitted experimental data of linear absorption very well.

After the coupling effect, the peak at 404 nm quenched and the peak at 320 nm blue shifted to 301 nm (Fig. 4c). The result meant that the main π-conjugated chain and the phenothiazine fragment were strongly affected during the coupling process. Meanwhile, there existed a new peak centred at 375 nm, which

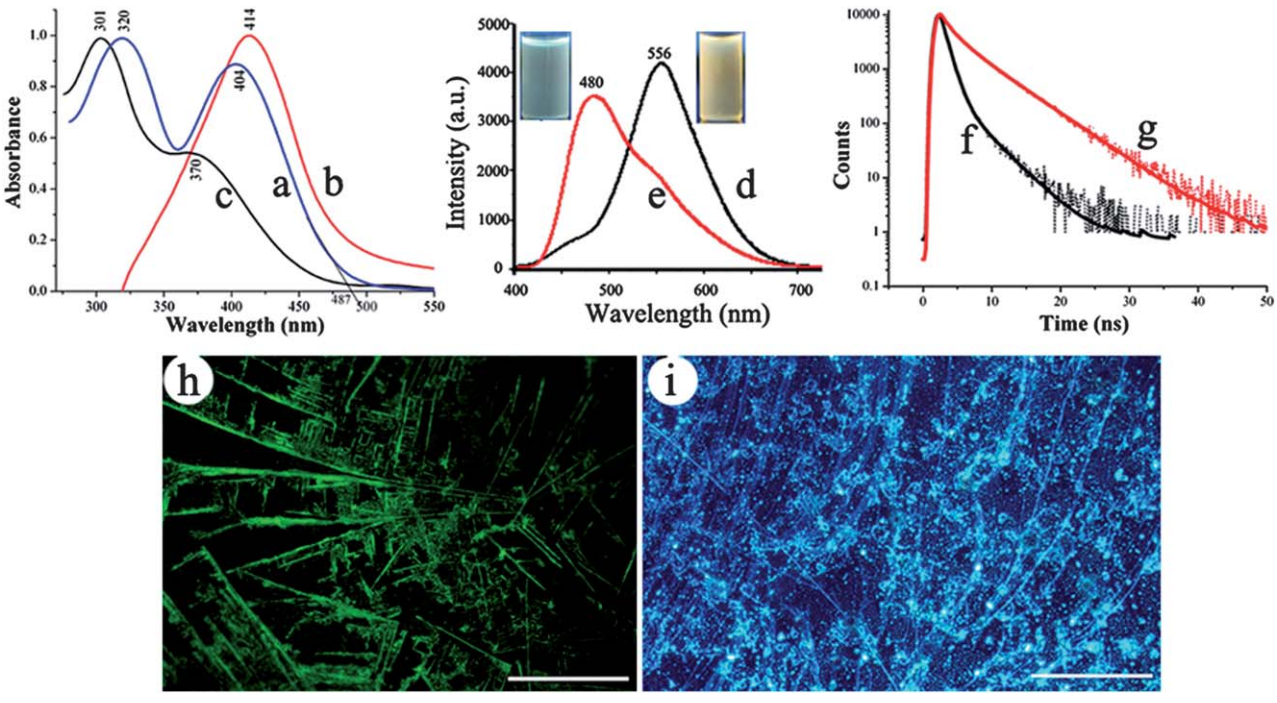

Fig. 4 UV-vis spectra of (a) pure **L**, (b) pure Ag NPs, and (c) **L**–Ag nanohybrid; fluorescence spectra of (d) **L** and (e) **L**–Ag nanohybrid; time-domain fluorescence intensity decay of (f) **L** and (g) **L**–Ag nanohybrid; fluorescence microscopy images of **L** (h) and **L**–Ag nanohybrid (i) with scar bars being 1 μm.

can be regarded as the inherent absorption band of the nanohybrid with a blue-shift from that of pure Ag NPs (414 nm, Fig. 4b) for ~39 nm, or a blue-shift from that of pure **L** for ~29 nm. The blue-shift might arise from the interactions between the newly produced **L** nanoribbons and Ag NPs *in situ*. The non-symmetric wide surface plasmon resonance (SPR) bands for both **L**–Ag nanohybrid and pure Ag NPs were elucidated based on a broadened size distribution, which was consistent with SEM results.

3.5.2 Fluorescent emission. The fluorescence spectrum of **L** nanoribbons displayed a clear yellow emission peak at 556 nm (Fig. 4d) attributing to the typical HOMO–LUMO transition of **L**,[21] which was quenched to be a shoulder band after the nanohybrid was obtained, and a new band appeared at 480 nm (blue emission) as shown in Fig. 4e (blue-shifted for 76 nm from that of **L**). Such an emission feature was observed only for the nanohybrid formed *in situ* but not for the physically mixed two components, from which only **L** fluorescence emission with quenched intensity was observed. The results revealed the existence of strong interactions between **L** and Ag NPs.

The quenched fluorescence band at 556 nm was attributed to the energy transfer from **L** to Ag NPs.[22] While the new bands for the nanohybrid (375 nm for absorption and 480 nm for emission) were attributed to the inherent absorption and emission of the corresponding nanohybrid, which were resulted from the electromagnetic coupling effect between the two components. Meanwhile, electron redistribution was a fundamental effect at the interface. That is to say, the Fermi energy level of Ag NPs should match the excited-state potential of **L**, the lowest unoccupied molecular orbital (LUMO) and the highest occupied molecular orbital (HOMO) included. When the two components were in close contact, the photogenerated electrons would be distributed between them. Thus, the intramolecular charge transfer (ICT) within the dye platform changed, which then promoted a change in the absorption and emission wavelengths. Furthermore, based on the redistribution of electrons at the interface, a new D–A system formed, in which **L** provided electrons, while the metal ions existing on the surface of the Ag NPs served as the electron acceptor. The new bands for the absorption and emission were attributed to the inherent optical properties of the newly formed D–A system, which was further approved from time-resolved fluorescence decay profile measurements.

3.5.3 Time resolved measurements. In this part, fluorescence decay profile measurements were carried out to study the difference between the spectral features of **L** and **L**–Ag nanohybrid. The decay profiles of **L** nanoribbons and the corresponding nanohybrid are shown in Fig. 4f and g. Table 3 contained pertinent fitting parameters obtained for each decay curve, including the fluorescence decay lifetime (τ), the corresponding amplitude (A) and the average amplitude-weighted lifetime ($\bar{\tau}$).

The FL lifetime of **L** nanoribbons (Fig. 4f) was 0.89 ns, and the fluorescence was found to decay with two components, which indicated that there existed two kinds of fluorescent components.[23] The result was in accordance with the two kinds of absorption bands shown in Fig. 4a and the calculated results mentioned above. A short component had a decay lifetime of 0.84 ns (98%), and the following component had 3.37 ns (2%). Meanwhile, for the **L**–Ag nanohybrid, the average FL lifetime was 2.58 ns (Fig. 4g), which was significantly longer than that of **L** nanoribbons. The fluorescence of the nanohybrid was decayed with three components. Compared to that of **L** nanoribbons, the corresponding amplitude (A) of a short component (0.82 ns) sharply decreased from 98% to 38%. At the same time, a new component appeared with the fluorescence decay lifetime and the amplitude being 5.11 ns and 33%, respectively.

The results confirmed the existence of a new fluorophore system in the nanohybrid, as discussed previously. However, the emission band of **L** and the nanobybrid showed only one peak. In the case of this point, the intense of the other bands should overlap the existing band or they appeared as a shoulder band. Moreover, the **L**–Ag nanohybrid seemed to provide a more stable environment for the excited state than pure **L**. The increase in τ suggested that the coupling of **L** and Ag NPs accelerated the yield of electron decay, which resulted in slower decay and a longer average fluorescence decay lifetime.

In general, the lifetime of fluorophores is inversely proportional to the total decay rate (k_t^0), which is the sum of the radiative decay rate (k_{rad}^0) and the nonradiative decay rate (k_{nr}^0).[24] When the fluorophores are in close contact with metal NPs, surface plasmons of metal NPs can affect the intrinsic radiative and/or nonradiative decay rate of the fluorophores. In this study, the prolonged lifetime indicated that either k_{rad}^0 or k_{nr}^0 was decreased after the coupling effect.[25] As quenched **L** emission was observed as shown in Fig. 4e, the prolonged lifetime of the **L**–Ag nanohybrid can be attributed to a decreased radiative decay rate. The newly appeared component (with decay lifetime being 5.11 ns) revealed the existence of a new fluorophore system, the radiative decay rate of which was slower than that of the other two components, which was responsible for the decreased radiative decay rate of the whole nanohybrid.

3.5.4 Fluorescence microscopy. As discussed above, the band at 480 nm for the **L**–Ag nanohybrid was the inherent fluorescent emission of the whole hybrid. The new emission band may come from the electromagnetic coupling effect between the two components, which would lead to the new fluorophore formation. The fluorescence microscopy might provide some clues to understand the mechanism.[26] Under the fluorescence microscope, pure **L** nanoribbons showed yellow emission, the length of which was ~2 μm (Fig. 4h). Pure Ag NPs prepared in the present work did not emit fluorescence under the same experimental conditions. While for the nanohybrid (Fig. 4i), the whole nanohybrid (**L** and Ag were included) showed blue fluorescence. Ag NPs were distributed throughout the surface of **L**, indicating their interfacial deposition under the surface of **L** nanoribbons.[27] The results revealed the existence of

Table 3 Fluorescence decay lifetime (τ) and amplitude (A) of fluorescence of **L** and **L**–Ag nanohybrid

	τ1 (ns)	A1 (%)	τ2 (ns)	A2 (%)	τ3 (ns)	A3 (%)	$\bar{\tau}$ (ns)	χ^2
L	0.84	98	3.37	2	—	—	0.89	1.03
L–Ag	0.82	38	2.06	29	5.11	33	2.58	0.98

the **L**–Ag hybrid as a new fluorophore, among which **L** interacted directly with Ag NPs and led to a new emission band.

3.6 Determination of interaction 'hot spot' at the interface

3.6.1 ^{1}H NMR spectroscopy. To further study the spectral features of the nanohybrid, the structure at the interface and the interaction 'hot spot' between **L** and Ag were investigated. Advanced spectroscopy experiments (such as Raman scattering and NMR methods) can bring about exciting photophysical properties and provide clues to gain deep insights into the electronic structure at the interface and recombination dynamics of the formation process of the dye–metal nanohybrid.

In the organic–metal nanohybrid systems, the binding effect at the organic–metal interface may cause changes in the chemical shift in the NMR spectra.[28] Thus, ^{1}H NMR spectroscopy can be used as a credible method to study the interface structure of such a nanohybrid.[2,29] Here, the ^{1}H NMR spectra of **L** before and after the coupling process were discussed in detail as follows.

Fig. S7† showed several differences between ^{1}H NMR spectra of the aromatic/alkene moieties (phenothiazine, benzyl, vinyl) of **L** in pure and hybrid states. The main differences in peak shifts of the aromatic/alkene moieties were clearly observed. This was particularly evident in the aromatic region, where proton peaks of the phenothiazine group shifted upfield, especially for the protons near S atoms. The upfield shift of proton c was the greatest (Δ = +0.03 ppm). The results indicated that the density of the electron cloud near S atoms decreased in the hybrid. At the other side, the aldehyde group and the aromatic moiety attached closely to the aldehyde group did not exhibit shift of their ^{1}H NMR chemical shifts, such as proton a, which indicated that the density of the electron cloud near the O atom was not perturbed in the hybrid.[30] Meanwhile, ^{1}H NMR chemical shifts were not changed for the physically mixed Ag NPs and **L**. The observations revealed that Ag NPs influenced intramolecular charge transfer (ICT) of **L**, and further confirmed that the coupling interaction between **L** and Ag NPs took place through the phenothiazine group, the strongest interaction occurred between S atoms and Ag.

The results mentioned above revealed that the coupling interaction between organic and inorganic components was the key factor to tune the optical property. **L** interacted with Ag NPs through S atoms of the phenothiazine group, which can change the charge recombination of **L** molecules at the interface, decrease the density of the electron cloud of the phenothiazine group and further decrease the electron donor effect of **L**. Thus, a quenched and blue-shifted fluorescence was observed. The above explanations were further supported by the results of Surface Enhanced Raman Scattering (SERS) as follows.

3.6.2 Surface enhanced Raman scattering. Being a powerful technique for determining structural information about a system, Raman scattering analysis was also an effective method to investigate the 'hot spot' functional group through which the organic agents can interact with a metal. In this part, the 'hot spot' functional group was determined by comparing relative intensities and frequency shifts of the Raman bands of **L** in the nanohybrid with respect to the corresponding Raman bands of the free molecule.

The Raman spectra of free **L** and the corresponding nanohybrid are given in Fig. 5. Compared to the normal Raman scattering (NRS) of **L**, the Raman scattering of **L** in the nanohybrid was enhanced. For example, the bands ranging from 1013 cm^{-1} to 1468 cm^{-1} were sharply enhanced, which were assigned to stretching vibration of the phenothiazine group and the C–H stretch band (see ESI, Fig. S8†). The large enhancement factors resulted from the coupling of the localized surface plasmon (LSP) of Ag NPs and the enhanced electromagnetic field intensity localized at the interface.[31] Besides the enhancement, some differences between the spectra were also observed. The band at 1044 cm^{-1} downshifted by 31 cm^{-1} to 1013 cm^{-1}, which was attributed to the symmetric C–S–C stretch. The band at 1200 cm^{-1} downshifted by 25 cm^{-1} to 1175 cm^{-1}, which was attributed to the asymmetric stretch of C–S–C. However, it was also noticed that the bands at 1598 and 1631 cm^{-1} changed little after hybrid formation. The two bands were attributed to the asymmetric and symmetric C=C stretch of the benzene ring and C=O stretch.[32] The results indicated that the aldehyde group and the adjacent benzene ring were not the 'hot spot' of **L**–Ag interaction. The results mentioned above revealed that the interactions between **L** and Ag NPs at the interface took place through S atoms of the phenothiazine group, which can explain the change in optical properties before and after the coupling process. The large enhancement factors may be due to the coupling of the LSP of Ag NPs and the enhanced electromagnetic field intensity localized at nanoparticle junctions.[33] The interactions further influenced the electron distribution of **L**, and decreased the electron cloud density of the phenothiazine group, especially that near S atoms, which accounted for the changes observed in H NMR and Raman spectra.[34] Furthermore, according to the Hard–Soft Acid–Base principle, Ag^+ ions at the interface should have more tendency to combine with S atoms. Therefore, in the case of **L**, a phenothiazine derivative as discussed above, the interactions between S atoms of it and Ag NPs led to the decrease of the electron cloud density of the electron-donor unit (phenothiazine group), and brought about the blue-shift of the fluorescence.

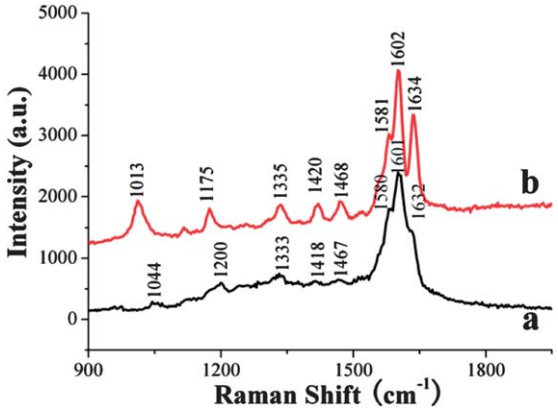

Fig. 5 Comparisons of NRS and SERS spectra of (a) **L** (×60) and (b) **L**–Ag nanohybrid.

Besides the effect of the coupling unit on interactions at the **L**–Ag interface, the energy-matching effect may be another important factor in distributing the photogenerated electrons at the interface, which was also a key matter in constructing dye–metal hybrids to tune the optical properties. That is to say, the band gap of Ag NPs should match the excited-state potential of **L**, including the lowest unoccupied molecular orbital (LUMO, the 'conduction band') and the highest occupied molecular orbital (HOMO, the 'valence band') of **L**. As a consequence, theoretical studies (mentioned previously) and electrochemical analysis of **L** have been used to gain insight into the differences between their apparent energy gaps.

3.7 Electrochemical property

To further study the energy gap between **L** and Ag, **L** had been analyzed by cyclic voltammetry in the presence of Bu_4NClO_4 (TBAP, 0.1 M) as a supporting electrolyte with a scan rate of 50 mV s^{-1} using a calomel electrode as a reference electrode.[35] Due to the presence of strong electron donor moieties and aldehyde unit in **L**, in CV experiments they displayed complex redox behavior involving multistep oxidation processes as shown in Fig. 6a. The first onset oxidation potential of **L** was 0.67 V, which can be identified as the oxidation of the phenothiazine fragment (ESI Fig. S9†). The estimated HOMO level in vacuum was −5.05 eV ($E_{HOMO} = -e(E_{onset} + 4.38)$ eV), which was in good agreement with the results from the theoretical calculation and the HOMO level was also close to the Fermi level of Ag.

A HOMO–LUMO gap of 2.55 eV of **L** was estimated from the absorption edge (λ_{edge} = 487 nm as shown in Fig. 4a). The LUMO energy level was calculated to be −3.50 eV by subtraction of the optical band gap from the HOMO energy levels ($E_{LUMO} = E_{HOMO} + E_{opt}$). The second oxidation potential of **L** was 1.16 V, which can be identified as the oxidation of the aldehyde group. The two oxidation potentials were much higher than that of the Ag^+/Ag electrode (0.2 V as shown in Fig. S10†). The results revealed the stability of **L** in $AgNO_3$–DMF solution. The electronic levels of **L** and the relative position of the Fermi level of Ag were also depicted in Fig. 6b.

Furthermore, the TD-DFT results also showed difference between the Fermi level of Ag and the HOMO–LUMO level of **L**. The calculated results are also listed in Fig. 6b. The LUMO level of **L** was calculated to be −2.08 eV. The HOMO level of **L** was −5.08 eV, which was close to the Fermi level of Ag (−4.26 eV) and also close to the data calculated from the first onset oxidation potential mentioned above. Thus, when **L** and Ag are in close contact, the electron redistribution may occur and the change of optical properties may appear.

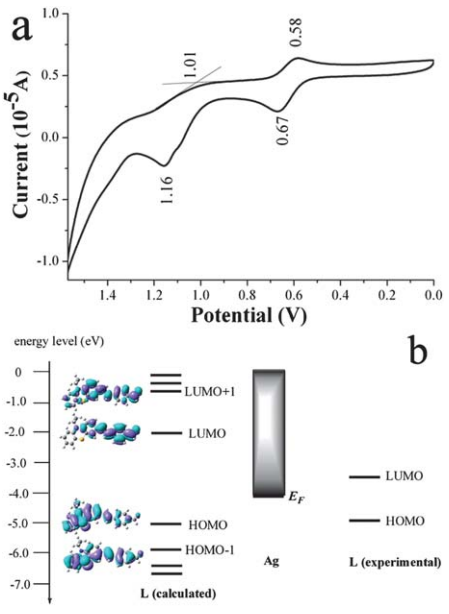

Fig. 6 (a) Cyclic-voltammetric response of **L** in the presence of 0.1 M TBAP *vs.* Ag/AgCl at room temperature. Scan rate: 50 mV s^{-1}; (b) calculated frontier orbitals and the corresponding energy of **L** in the gas phase and electronic energy level alignments for Ag and **L** (both from calculated and experimental data).

3.8 Effect of concentration of $AgNO_3$ on the optical properties of L–Ag nanohybrids

To evaluate the effect of the molar ratio between **L** and Ag, various amounts of $AgNO_3$ were used under otherwise identical conditions.

It was found that the concentration of $AgNO_3$ used in the preparation process influenced the photophysical properties of the nanohybrid and did not change the basic features of their morphology. In this process, the usage of **L** was fixed at 0.01 mmol, and the usage of $AgNO_3$ was 0.002 mmol, 0.005 mmol, 0.01 mmol and 0.1 mmol, respectively. The UV-vis absorption spectra (Fig. S11†) showed that the usage of $AgNO_3$ affected the optical properties of the nanohybrid. When the usage of $AgNO_3$ was 0.002 mmol (the molar ratio of **L** to Ag is 5 : 1), the nanohybrid exhibited a major absorption peak at 386 nm (Fig. S11d†), which was blue-shifted for 18 nm from 404 nm of pure **L** (Fig. 3a). As the usage of $AgNO_3$ increased, the major absorption peak showed a continuous blue shift. When the molar ratio of **L** to Ag was 2 : 1, the major absorption peak was about 380 nm (Fig. S11c†). When the ratio was 1 : 1, the peak was 370 nm (Fig. S11b† and 4c). When the ratio changed to 1 : 10, the peak blue-shifted to 366 nm (Fig. S11a†) (for about 40 nm blue-shift compared to pure **L**). The results revealed that with higher proportion of Ag in the hybrid, there existed higher influence on UV-vis absorption of **L**. This blue shift might arise from the interactions between newly produced **L** nanoribbons and Ag NPs *in situ.*

The usage of Ag also influenced the fluorescence spectrum of the hybrid. The fluorescence spectrum of pure **L** displayed an emission peak at 556 nm as shown in Fig. 4d. When **L** coupled with Ag NPs, the emission was partially quenched and new bands with different degrees of blue-shift appeared (Fig. 7b–f). When the molar ratio of **L** to Ag was 5 : 1, except for characteristic emission of **L**, there also existed a shoulder peak at 490 nm (Fig. 7b). The ratio of the emission intensity at 490 nm to that at 556 nm was 0.23. When the usage of Ag increased to $n_L : n_{Ag} = 2 : 1$, apparent bimodal emission peaks appeared, a new emission band at 470 nm appeared, with the ratio of I_{470} to I_{560} as 0.93 : 1. When the molar ratio of **L** to Ag further increased

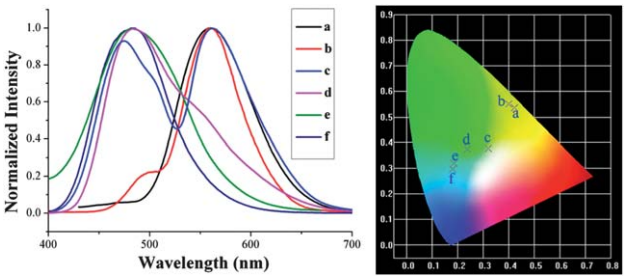

Fig. 7 Fluorescence spectra of **L**–Ag nanohybrids prepared with different molar ratios of **L**–Ag: (a) **L**; (b) **L** : Ag = 5 : 1; (c) **L** : Ag = 2 : 1; (d) **L** : Ag = 1 : 1; (e) **L** : Ag = 1 : 3; (f) **L** : Ag = 1 : 10.

to 1 : 1, the hybrid mainly showed new emission, which was centered at about 480 nm, while the characteristic emission peak of **L** was only a shoulder peak. When the usage of Ag increases to $n_L : n_{Ag} = 1 : 10$, the characteristic emission peak of **L** did not appear. The product exhibited emission at 480 nm for the whole nanohybrid.

3.9 Antibacterial effect

In this study, besides the interesting optical properties, the interactions of **L** and Ag at the interface also brought about the improvement of antibacterial effects. The antibacterial effects of **L**, Ag NP and **L**–Ag nanohybrid were investigated by two methods, one was paper disk diffusion assay and the other was minimal inhibitory concentration (MIC).

For disk diffusion assay, the size of the zone of inhibition can be clearly seen from the bright field images in Fig. 8a and b. As for *E. coli*, the diameter of the zone of inhibition for **L** was ~1.0 mm (Fig. 8a), which was ~2.6 mm for Ag NPs (Fig. S14†). The diameter extended to about 5.0 mm for the nanohybrid (Fig. 8b). As for *S. aureus*, the diameter of the zone of inhibition for **L** nanoribbon disks was approximately 2.7 mm (Fig. S13a†). It was approximately 2.5 mm for Ag NPs (Fig. S14†), while it was about 3.2 mm for the nanohybrid (Fig. S13b†). The mixture of physically mixed **L** nanoribbons and Ag NPs also reflected a small enhancement effect to some extent. The diameter of the inhibition zone for the mixture was ~2.8 mm for *S. aureus* and ~3.5 mm for *E. coli*, respectively, as shown in Fig. S15.†

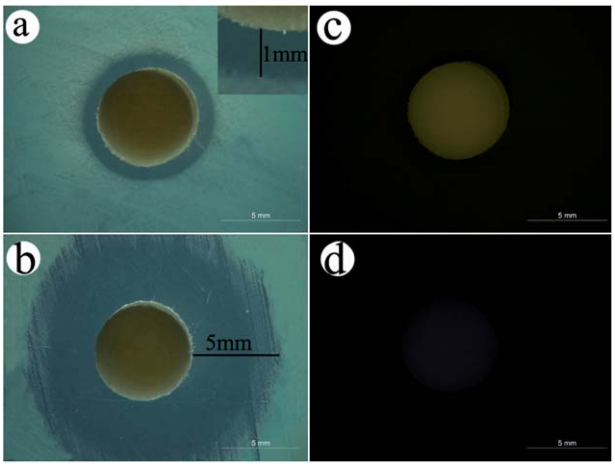

Fig. 8 Photograph images of the zone of inhibition of *E. coli*. (a) and (b) bright-field image of **L** and **L**–Ag nanohybrid, respectively; (c) and (d) fluorescence microscopy of (a) and (b) respectively.

These results indicated that, the **L**–Ag nanohybrid exhibited superior performance as an antibacterial agent compared to either pure Ag or pure **L**. There were several explanations to understand the phenomenon. Firstly, the antibacterial activity of Ag NPs was influenced by the size of the particles: the smaller the particles, the greater the antibacterial effect.[36] The size of Ag in the **L**–Ag nanohybrid was smaller than that of pure Ag NCs, which can improve the antibacterial property of the whole nanohybrid. Secondly, as mentioned above, the Ag NPs in the **L**–Ag nanohybrid had an excellent dispersibility, which will result in strong adsorption ability among the bacteria, Ag NPs and **L**. As a consequence, the bacteria had more opportunities to contact with Ag NPs and **L**, which was regarded to be advantageous to improve the antibacterial activity.[37] Thirdly, as **L** was a molecule rich in negative charge, when **L** coupled with Ag NPs, the concentration of Ag^+ at the interface was lower than that of pure Ag NPs, which may decrease the antibacterial activity.[38] However, the antibacterial effect of the nanohybrid was stronger than that of pure Ag NPs. In the case of this point, it was believed that the synergetic effects of both **L** and Ag phases might be responsible for the enhanced bactericidal activity of the nanohybrid against *E. coli* and/or *S. aureus*. That is to say, the synergistic effect between **L** and Ag caused the enhancement of the antibacterial ability.

The results of optical properties, TD-DFT calculation and electrochemical analysis mentioned above revealed that the changes in the optical properties were due to the coupling interactions and synergistic matching effects between the two components at the molecular level, through which it was natural to assume that the microscopic mechanism of enhanced antibacterial activity was also related to the synergistic matching effects, not just a simple physical mixture.

The fluorescence microscopy technique was used here to study the possible mechanism of the improvement.[39] As shown in Fig. 8c, S13c and d,† the diffusion of **L** in the bacteria was much weaker than the diffusion of the **L**–Ag nanohybrid in bacteria, which was thought to be the direct cause of the difference of the antibacterial ability.[40] As for **L**, the whole system showed clearly yellow fluorescence and the fluorescence intensity was somewhat high, which revealed that much of **L** still gathered on the filter paper disk and only a small amount of **L** diffused into the bacteria (both for *E. coli* and *S. aureus*). Thus, the diameter of the zone of inhibition for **L** might be small. In contrast, as for the **L**–Ag nanohybrid, the whole system showed weak blue emission. The result showed that a small amount of **L**–Ag nanohybrids still gathered on the filter paper disk while much of it diffused into the bacteria. In the case of this point, more released Ag^+ from the nanohybrid had the opportunity to act with the bacteria.[38,41] As a result, the antibacterial ability of the **L**–Ag nanohybrid might be strong and the diameter of the zone of inhibition would be extended. Here, the tunable fluorescence was used as a wavelength-based biodetection tool to study the mechanism. The synergistic effects between the

Table 4 Minimum inhibitory concentration tests against *E. coli*[a]

		Concentration of the samples (mg mL^{-1})									
Sample	Microorganism	500	250	125	62.5	31.25	15.63	7.81	3.91	1.95	0.98
L	*E. coli*	−	−	−	−	±	+	+	+	+	+
Ag	*E. coli*	−	−	−	−	−	−	−	±	+	+
L–Ag	*E. coli*	−	−	−	−	−	−	−	−	−	+

[a] Liquid media is clear before incubation of *E. coli*, '−' no growth, '+' growth.

components acted on both the photophysical properties and the bioactivity, which meant that the photophysical properties can be applied in bio- and chemical sensing and can be used as a new type of optical device to study the bioactivity.

In the following research, the MIC method was used to test the growth inhibition effects for *E. coli* as **L**–Ag nanohybrids showed higher bactericidal activity against *E. coli* than *S. aureus.* **L** nanoribbons, Ag NPs and **L**–Ag nanohybrids were studied respectively. The samples were firstly dispersed into high-purity water, then diluted 2–1024 times with 100 μL of Mueller-Hinton broth inoculated with the tested bacteria at a concentration of 9 × 10^4 CFU mL^{-1}. The MIC value was measured after 24 h of incubation at 37 °C. Growth or no-growth was determined by visual inspection. The representative photographs of the test against *E. coli* are listed in the ESI (Fig. S16†). High antibacterial activities against the bacteria are shown in Table 4. The MIC of the nanohybrid was about 1.95 μg mL^{-1}, which was about four times lower that of pure Ag NPs (7.81 μg mL^{-1}) and about 32 times lower than that of pure **L** (62.5 μg mL^{-1}) after 24 h incubation. Notably, the **L**–Ag nanohybrid exhibited enhanced antibacterial activity compared to both pure **L** and pure Ag.

The results of antibacterial assay suggested that the as-prepared **L**–Ag nanohybrid had potential application in anti-adhesion. We therefore proposed its potential application in fabricating other silver-loaded antibacterial organic–metal nanohybrid materials.

4 Conclusion

In this work, an organic–metal nanohybrid (**L**–Ag nanohybrid) was designed and prepared. **L** coupled with Ag NPs *via* the electron-donor unit and resulted in a significant blue-shift of the fluorescence, an obvious increase of FL lifetime. The energy match between the Fermi level of Ag NPs and the frontier molecular orbital energy of **L** was an effective factor in distributing the photogenerated electrons at the interface and in constructing the **L**–Ag nanohybrid to tune the optical properties. The week interactions between the two components also brought about an improvement in antibacterial activity against both bacteria *E. coli* and *S. aureus* compared to either pure Ag NPs or pure **L**. The tunable fluorescence was used as a wavelength-based biodetection tool to study the mechanism of enhanced antibacterial activity. The energy transfer between the components, the tunable optical properties and the application for antibacterial activity made the **L**–Ag nanohybrid intrinsically interesting for further spectral and/or biological studies.

Acknowledgements

This work was supported by the NSFC (no.: 21071001, 21271004, 21101001, 21271003), the Natural Science Foundation of Anhui Province (1208085MB22), Focus on returned overseas scholar of Ministry of Education of China and New Century Excellent Talents in University (China).

Notes and references

1 S. Murphy, L. Huang and P. V. Kamat, *J. Phys. Chem. C*, 2011, **115**, 22761–22769; N. Kometani, M. Tsubonishi, T. Fujita, K. Asami and Y. Yonezawa, *Langmuir*, 2001, **17**, 578–580; H. Nabika, M. Takase, F. Nagasawa and K. Murakoshi, *J. Phys. Chem. Lett.*, 2010, **1**, 2470–2487; J. Lee, P. Hernandez, J. Lee, A. O. Govorov and N. A. Kotov, *Nat. Mater.*, 2007, **6**, 291–295.

2 Y. H. Gao, J. Y. Wu, Q. Zhao, L. X. Zheng, H. P. Zhou, S. Y. Zhang, J. X. Yang and Y. P. Tian, *New J. Chem.*, 2009, **33**, 607–611; K. S. Kim, J. H. Kim, H. Kim, F. Laquai, E. Arifin, J. K. Lee, S. Yoo and B. H. Sohn, *ACS Nano*, 2012, **6**, 5051–5059.

3 Y. Sun, *J. Phys. Chem. C*, 2010, **114**, 2127–2133.

4 D. L. Chen, S. H. Yoo, Q. S. Huang, G. Ali and S. O. Cho, *Chem.–Eur. J.*, 2012, **18**, 5192–5200.

5 Z. A. Tagar, S. N. Memon, M. H. Agheem, Y. Junejo, S. S. Hassan, N. H. Kalwar and M. I. Khattak, *Sens. Actuators, B*, 2011, **157**, 430–437; J. Puišo, J. Laurikaitien, D. Adlienè and I. Prosyčeva, *Radiat. Prot. Dosim.*, 2010, **139**, 353–356.

6 J. Yan, X. Han, J. He, L. Kang, B. Zhang, Y. Du, H. Zhao, C. Dong, H. L. Wang and P. Xu, *ACS Appl. Mater. Interfaces*, 2012, **4**, 2752–2756; E. Papadopoulou and S. E. J. Bell, *Chem.–Eur. J.*, 2012, **18**, 5394–5400.

7 X. Huang, S. Neretina and M. A. El-Sayed, *Adv. Mater.*, 2009, **21**, 4880–4910; X. Huang, I. H. El-Sayed, W. Qian and M. A. El-Sayed, *J. Am. Chem. Soc.*, 2006, **128**, 2115–2120; J. Z. Zhang, *J. Phys. Chem. Lett.*, 2010, **1**, 686–695; H. J. Parab, H. M. Chen, T. Lai, J. H. Huang, P. H. Chen, R. Liu, M. Hsiao, C. Chen, D. Tsai and Y. Hwu, *J. Phys. Chem. C*, 2009, **113**, 7574–7578.

8 S. Pal, Y. K. Tak and J. M. Song, *Appl. Environ. Microbiol.*, 2007, **73**, 1712–1720.

9 P. Singh, K. L. Parent and D. A. Buttry, *J. Am. Chem. Soc.*, 2012, **134**, 5610–5617; Y. Wang, J. Zhang, L. Huang, D. He,

L. Ma, J. Ouyang and F. Jiang, *Chem.–Eur. J.*, 2012, **18**, 1432–1437.
10 J. H. Lee, G. H. Kim and J. M. Nam, *J. Am. Chem. Soc.*, 2012, **134**, 5456–5459.
11 G. W. Kim, M. J. Cho and Y. J. Yu, *Chem. Mater.*, 2007, **19**, 42–50.
12 M. Wainwright, L. Amaral and J. E. Kristiansen, *Open J. Pharmacology*, 2012, 2–1.
13 X. Zhang, Y. Xie, W. Yu, Q. Zhao, M. H. Jiang and Y. P. Tian, *Inorg. Chem.*, 2003, **42**, 3734–3737; D. M. Li, X. H. Tian, G. J. Hu, Q. Zhang, P. Wang, P. P. Sun, H. P. Zhou, X. M. Meng, J. X. Yang, J. Y. Wu, B. K. Jin, S. Y. Zhang, X. T. Tao and Y. P. Tian, *Inorg. Chem.*, 2011, **50**, 7997–8006; X. C. Wang, Y. P. Tian, Y. H. Kan, C. Y. Zuo, J. Y. Wu, B. K. Jin, H. P. Zhou, J. X. Yang, S. Y. Zhang, X. T. Tao and M. H. Jiang, *Dalton Trans.*, 2009, 4096–4103.
14 L. Kong, J. X. Yang, X. P. Hao, H. P. Zhou, J. Y. Wu, F. Y. Hao, L. Li, S. Y. Zhang, B. K. Jin, X. T. Tao, M. H. Jiang and Y. P. Tian, *J. Mater. Chem.*, 2010, **20**, 7372–7377.
15 M. J. G. W. T. Frisch, H. B. Schlegel, G. E. Scuseria, M. A. Robb, J. R. Cheeseman, G. Scalmani, V. Barone, B. Mennucci, G. A. Petersson, H. Nakatsuji, M. Caricato, X. Li, H. P. Hratchian, A. F. Izmaylov, J. Bloino, G. Zheng, J. L. Sonnenberg, M. Hada, M. Ehara, K. Toyota, R. Fukuda, J. Hasegawa, M. Ishida, T. Nakajima, Y. Honda, O. Kitao, H. Nakai, T. Vreven, J. A. Montgomery, Jr, J. E. Peralta, F. Ogliaro, M. Bearpark, J. J. Heyd, E. Brothers, K. N. Kudin, V. N. Staroverov, R. Kobayashi, J. Normand, K. Raghavachari, A. Rendell, J. C. Burant, S. S. Iyengar, J. Tomasi, M. Cossi, N. Rega, J. M. Millam, M. Klene, J. E. Knox, J. B. Cross, V. Bakken, C. Adamo, J. Jaramillo, R. Gomperts, R. E. Stratmann, O. Yazyev, A. J. Austin, R. Cammi, C. Pomelli, J. W. Ochterski, R. L. Martin, K. Morokuma, V. G. Zakrzewski, G. A. Voth, P. Salvador, J. J. Dannenberg, S. Dapprich, A. D. Daniels, O. Farkas, J. B. Foresman, J. V. Ortiz, J. Cioslowski and D. J. Fox, *Gaussian 09, Revision B. 01*, Gaussian, Inc., Wallingford CT, 2009.
16 S. Grimme, *Comput. Mol. Sci.*, 2011, 211–228; Y. Zhao and D. G. Truhlar, *Theor. Chem. Acc.*, 2008, **120**, 215–241.
17 B. Paizs and S. Suhai, *J. Comput. Chem.*, 1998, **19**, 575–584; I. R. Could and P. A. Kollman, *J. Am. Chem. Soc.*, 1994, **116**, 2493–2499.
18 G. M. Sheldrick, *SHELXTL V5.1 Software Reference Manual*, Bruker, AXS Inc., Madison, Wisconsin, USA, 1997.
19 V. G. Pol, D. N. Srivastava, O. Palchik, V. Palchik, M. A. Slifkin, A. M. Weiss and A. Gedanken, *Langmuir*, 2002, **18**, 3352–3357.
20 Z. He, C. W. Kan, C. L. Ho, W. Y. Wong, C. H. Chui, K. L. Tong, S. K. So, T. H. Lee, L. M. Leung and Z. Y. Lin, *Dyes Pigm.*, 2011, **88**, 333–343.
21 H. P. Zhou, P. Wang, L. X. Zheng, W. Q. Geng, J. H. Yin, X. P. Gan, G. Y. Xu, J. Y. Wu, Y. P. Tian, Y. H. Kan, X. T. Tao and M. H. Jiang, *J. Phys. Chem. A*, 2009, **113**, 2584–2590.
22 Z. H. Nie, A. Petukhova and E. Kumacheva, *Nat. Nanotechnol.*, 2010, **5**, 15–25.
23 J. R. Casanova-Moreno and D. Bizzotto, *Langmuir*, 2013, **29**, 2065–2074.
24 K. S. Kim, J. H. Kim, H. Kim, F. Laquai, E. Arifin, J. K. Lee, S. I. Yoo and B. H. Sohn, *ACS Nano*, 2012, **6**, 5051–5059.
25 E. Dulkeith, A. C. Morteani, T. Niedereichholz, T. A. Klar, J. Feldmann, S. A. Levi, F. C. J. M. van Veggel, D. N. Reinhoudt, M. Möller and D. I. Gittins, *Phys. Rev. Lett.*, 2002, **89**, 203002.
26 J. C. Vaughan, G. T. Dempsey, E. Sun and X. W. Zhuang, *J. Am. Chem. Soc.*, 2013, **135**, 1197–1200.
27 K. Goto, R. Omae, M. Yamaji and T. Shinmyozu, *J. Photochem. Photobiol., A*, 2008, **194**, 92–96.
28 F. Porta, Z. Krpetić, L. Prati, A. Gaiassi and G. Scarić, *Langmuir*, 2008, **24**, 7061–7064; C. Querner, P. Reiss, J. Bleuse and A. Pron, *J. Am. Chem. Soc.*, 2004, **126**, 11574–11582; C. Querner, A. Benedetto, R. Demadrille, P. Rannou and P. Reiss, *Chem. Mater.*, 2006, **18**, 4817–4826; H. F. Qian, M. Z. Zhu, C. Gayathri, R. R. Gil and R. C. Jin, *ACS Nano*, 2011, **5**, 8935–8942.
29 K. Salorinne, T. Lahtinen, J. Koivisto, E. Kalenius, M. Nissinen, M. Pettersson and H. Häkkinen, *Anal. Chem.*, 2013, **85**, 3489–3492.
30 P. M. S. Pulkkinen, S. Wiktorowicz, V. Aseyev and H. Tenhu, *RSC Adv.*, 2013, **3**, 733–742.
31 M. P. Singh and G. F. Strouse, *J. Am. Chem. Soc.*, 2010, **132**, 9383–9391; M. López-López, J. L. Ferrando and C. García-Ruiz, *Anal. Chem.*, 2013, **85**, 2595–2600.
32 S. Y. Lin, W. Q. Zhu, Y. H. Jin and K. B. Crozier, *Nano Lett.*, 2013, **13**, 559–563.
33 M. Wang, T. Teslova, F. Xu, T. Spataru, J. R. Lombardi and R. L. Birke, *J. Phys. Chem. C*, 2007, **111**, 3038–3043.
34 S. T. Sivapalan, B. M. DeVetter, T. K. Yang, T. van Dijk, M. V. Schulmerich, P. S. Carney, R. Bhargava and C. J. Murphy, *ACS Nano*, 2013, **7**, 2099–2105; E. Cortés, P. G. Etchegoin, E. C. L. Ru, A. Fainstein, M. E. Vela and R. C. Salvarezza, *J. Am. Chem. Soc.*, 2013, **135**, 2809–2815; S. Sanchez-Cortes, R. M. Berenguel, A. Madejón and M. Pérez-Méndez, *Biomacromolecules*, 2002, **3**, 655.
35 T. Wang, S. Y. Zhang, C. J. Mao, J. M. Song, H. L. Niu, B. K. Jin and Y. P. Tian, *Biosens. Bioelectron.*, 2012, **31**, 369–375.
36 G. A. Sotiriou and S. E. Pratsinis, *Environ. Sci. Technol.*, 2010, **44**, 5649–5654; A. Panáček, L. Kvítek, R. Prucek, M. Kolář, R. Večeřová, N. Pizúrová, V. K. Sharma, T. Nevěčná and R. Zbořil, *J. Phys. Chem. B*, 2006, **110**, 16248–16253.
37 Y. H. Kim, D. K. Lee, H. G. Cha, C. W. Kim and Y. S. Kang, *J. Phys. Chem. C*, 2007, **111**, 3629–3635.
38 M. L. Pang, J. Y. Hu and H. C. Zeng, *J. Am. Chem. Soc.*, 2010, **132**, 10771–10785; Z. M. Xiu, Q. B. Zhang, H. L. Puppala, V. L. Colvin and P. J. J. Alvarez, *Nano Lett.*, 2012, **12**, 4271–4275.
39 N. G. Horton, K. Wang, D. Kobat, C. G. Clark, F. W. Wise, C. B. Schaffer and C. Xu, *Nat. Photonics*, 2013, **7**, 205–209.
40 C. V. Melo, M. Mele, M. Curcio, D. Comprido, C. G. Silva and C. B. Duarte, *PLoS One*, 2013, **8**, e53793.
41 M. L. Pang, J. Y. Hu and H. C. Zeng, *J. Am. Chem. Soc.*, 2010, **132**, 10771–10785.